

A FE² modelling approach to hydromechanical coupling in cracking-induced localization problems



A.P. van den Eijnden^{a,b,d,*}, P. Bésuelle^{c,b}, R. Chambon^b, F. Collin^d

^aAndra, 1/7 rue Jean Monnet, 92298 Châtenay-Malabry, France

^bUniv. Grenoble Alpes, 3SR, 38000, Grenoble, France

^cCNRS, 3SR, 38000 Grenoble, France

^dArGenCo dept, Univ. of Liège, 4000 Liège, Belgium

ARTICLE INFO

Article history:

Received 17 December 2015

Revised 17 June 2016

Available online 5 July 2016

Keywords:

Multiscale modelling

FE²

Computational homogenization

Hydromechanical coupling

Local second gradient model

Cracking-induced strain localization

ABSTRACT

An approach to multiscale modelling of the hydro-mechanical behaviour of geomaterials in the framework of computational homogenization is presented. At the micro level a representative elementary volume (REV) is used to model the material behaviour based on the interaction between a solid skeleton and a pore fluid to provide the global material responses and associated stiffness matrices. Computational homogenization is used to retrieve these stiffness matrices from the micro level. The global response to deformation of the REV serves as an implicit constitutive law for the macroscale. On the macroscale, a poro-mechanical continuum is defined with coupled hydro-mechanical behaviour, relying on the constitutive relations obtained from the modelling at the microscale. This double scale approach is applied in the simulation of a biaxial deformation tests and the response at the macro level is related to the micro-mechanical behaviour. Hydromechanical coupling is studied as well as material anisotropy. To be able to study localization of strain, the doublescale approach is coupled with a local second gradient paradigm to maintain mesh objectivity when shear bands develop.

© 2016 Elsevier Ltd. All rights reserved.

1. Introduction

The classical approach to modelling hydromechanical coupling in materials is the poromechanical description, founded on the pioneering work of Biot (1941), in which a solid and a fluid continuum exist at the same material point and the behaviour of both continua and their interaction are modelled by phenomenological relations (for details, developments and a review see Coussy (1995) and Schanz (2009)). The phenomenological relations of the poromechanical description are supposed to correctly represent the interaction between the solid skeleton and the pore fluid, that could be identified at a microscopic scale. These relations are readily available for cases in which material properties are constant, but for more complex behaviour, the formulation of constitutive relations and their implementation in numerical methods becomes more and more complex. An alternative approach to deriving the macroscale constitutive relations is to start from the underlying microstructural description, for which the different components of the material can be modelled explicitly and the interaction of the constituents can be defined based on physical considerations.

In this work, the framework of computational homogenization is used in the finite element squared (FE²) method. On a microscale level, the microstructure of the material is modelled in a representative elementary volume (REV), of which the homogenized response serves as a numerical constitutive relations in the macroscale continuum. This framework was initially introduced for the modelling of microstructural solids of different nature (Feyel and Chaboche, 2000; Kouznetsova et al., 2001; Miehe and Koch, 2002; Terada and Kikuchi, 1995, see also Schröder, 2014 for an extensive overview) and later extended to multiphysics couplings, starting with thermomechanical coupling by Özdemir et al. (2008a); 2008b). Aspects of hydromechanical coupling were studied using computational homogenization by Massart (Massart and Selvadurai, 2012; 2014), and doublescale computations with computational homogenization of hydromechanical coupled behaviour were studied in Mercatoris et al. (2014) and Jänicke et al. (2015).

These methods all describe first-order computational homogenization schemes, taking into account only the first gradient of the kinematics fields, which allows the full incorporation of the separation of scales. This means that the length scale of the kinematical gradients at the macroscale is much larger than the microstructural REV, such that the REV represents the material point behaviour. The result of the separation of scales is that no

* Corresponding author.

E-mail address: a.p.vandeneijnden@tudelft.nl (A.P. van den Eijnden).

macroscopic length scale can be taken into account and the method is limited to the classical continuum mechanics theory (Geers et al., 2010). As a result, a continuum approach has to be maintained at the macroscale throughout the computation. To overcome these limitations of the classical continuum theory, the method was extended to second-order computational homogenization (Feyel, 2003; Kouznetsova et al., 2004), deriving the classical part of the constitutive behaviour as well as the higher gradient part, thereby directly linking the length scales between micro and macroscale. With these enrichments, objectivity of the solutions with respect to the mesh was restored at the cost of losing the separation of scales.

Additional approaches were presented for micromorphic continua (Jänicke et al., 2009), while others have abandoned the macroscale continuum formulation and introduced discontinuous modes of deformation (Coenen et al., 2011a; Mercatoris and Marsart, 2011; Nguyen et al., 2011; Toro et al., 2014). However, the application of these discontinuous modes of deformation at the macroscale could lead to complications in case of multiphase couplings and the restriction to a macroscale continuum is therefore preferred in this work.

At the macroscale, difficulties arise in the classical formulation when softening response is to be considered, and the well-known mesh-sensitivity appears with the loss of ellipticity of the equilibrium equations (Pijaudier-Chabot and Bažant, 1987). To restore the well-posedness of the macroscale problem, an enrichment of the kinematical constraints is required. This enrichment has to allow the use of any classical constitutive relation, both for the mechanical and the hydraulic behaviour and its coupling, since the computational homogenization will provide a constitutive relation in the most general form.

In this work a computational homogenization approach is introduced for the homogenization of microscale solid-fluid interaction to obtain a macroscale poromechanical description. The microscale model is based on the work of Frey et al. (2012). It describes the interaction between the solid skeleton and pore fluid in a REV, without relying on phenomenological coupling relations at the microscale. For upscaling the hydromechanical coupled response to kinematic loading of the REV, the framework of computational homogenization (Kouznetsova et al., 2001) is extended to take into account the hydromechanical coupled behaviour. The resulting numerical constitutive relation is coupled with a local second gradient paradigm for hydromechanical coupling (Collin et al., 2006). With the decomposition assumption between first and second gradient parts of the constitutive equations (Chambon et al., 2001), the continuum can be combined with any classical constitutive relation for hydromechanical coupling.

The paper is structured as follows; Section 2 presents the macroscale formulation of the poromechanical continuum with the local second gradient model. Section 3 introduces the framework for the REV derived from the assumption of local periodicity and introduces the micromechanical model. Section 4 provides the formulation of the computational homogenization for hydromechanical coupling based on the Hill-Mandel macro-homogeneity principle to derive the definitions of homogenized macro response. An example of the application of the model is given in Section 5 on the modelling of biaxial compression under transient conditions. The paper closes with some concluding remarks in Section 6.

2. Macroscale formulation of the saturated poromechanical continuum in finite deformation

As it is the ambition to apply the method on localization problems with material softening, an enhancement of the macroscale continuum is required to maintain the objectivity of

the macroscale formulation in the softening domain. Many regularization methods were proposed for this purpose, either based on a nonlocal averaging (Pijaudier-Chabot and Bažant, 1987), gradient plasticity theories (Aifantis, 1984) or based on micromorphic media (Germain, 1973) of which many specific cases can be derived. The most famous of these cases is the micropolar continuum, better known as the Cosserat medium (Cosserat and Cosserat, 1909). Here, the local second gradient paradigm (Chambon and Caillerie, 1999; Germain, 1973; Matsushima et al., 2002) is chosen, which is a specific case of micromorphic medium in which the microkinematic gradient v_{ij} is constrained to be equal to the macro displacement gradient $\partial u_i / \partial x_j$. The weak form balance equation can be written with Lagrange multipliers to avoid the use of C^1 shape functions for the displacement fields (Chambon et al., 2001):

$$\int_{\Omega^t} \left(\sigma_{ij}^t \frac{\partial u_i^*}{\partial x_j^t} + \Sigma_{ijk}^t \frac{\partial v_{ij}^*}{\partial x_k^t} \right) d\Omega - \int_{\Omega^t} \lambda_{ij} \left(\frac{\partial u_i^*}{\partial x_j^t} - v_{ij}^* \right) d\Omega - \bar{W}_e^* = 0 \quad (1)$$

with \bar{W}_e^* the external virtual work as an effect of the boundary traction \bar{t} and the boundary double traction \bar{T} . Superscripts t and $*$ denote quantities at time t and virtual quantities respectively; σ_{ij}^t are the components of the Cauchy stress tensor, Σ_{ijk}^t are the components of the double stress tensor. In addition, the constraint on the microkinematical tensor \mathbf{v} , with components v_{ij} , requires the additional balance equation with respect to the Lagrange multiplier fields λ_{ij} :

$$\int_{\Omega^t} \lambda_{ij}^* \left(\frac{\partial u_i^t}{\partial x_j^t} - v_{ij}^t \right) d\Omega^t = 0 \quad (2)$$

The balance equation for the fluid part of the problem is formulated without the gradient enhancement. In absence of sink terms and neglecting gravitational influences, this gives:

$$\int_{\Omega^t} \left(\dot{M}^t p^* - m_i^t \frac{\partial p^*}{\partial x_i^t} \right) d\Omega - \bar{R}_e^* = 0 \quad (3)$$

where m_i^t are the components of the fluid mass flux. The external virtual work \bar{R}_e^* is the combined effort of the boundary fluid mass flux $\bar{m}^t = m_i n_i$ (n_i being the components of the boundary normal outward vector \bar{n}) and possible sink terms Q^t . M is the specific mass of the fluid phase with \dot{M} its time derivative and p is the pore pressure. The iterative search to a configuration Ω^t for which (1) to (3) hold entails looking for a configuration $\Omega^{\tau 2}$ that corrects for the residual terms $W_{res}^{\tau 1}$, $T_{res}^{\tau 1}$ and $R_{res}^{\tau 1}$ corresponding to (1), (2) and (3) respectively from a preceding test solution of configuration $\Omega^{\tau 1}$, using a full Newton-Raphson procedure. Development of the iterative procedure in an updated lagrangian formulation (with respect to configuration $\tau 1$), leads to the following combined expression of iterative update $d\Omega$ between $\Omega^{\tau 1}$ and $\Omega^{\tau 2}$ (see Matsushima et al., 2002 and Collin et al., 2006 for full details):

$$\int_{\Omega^{\tau 1}} [U_{(x,y)}^{*,\tau 1}] [E^{\tau 1}] [dU_{(x,y)}^{\tau 1}] d\Omega = -W_{res}^{\tau 1} - T_{res}^{\tau 1} - R_{res}^{\tau 1} \quad (4)$$

The column vector $[dU^{\tau 1}]$ contains subsequently the terms $\frac{\partial du_i^{\tau 1}}{\partial x_j^{\tau 1}}$, $\frac{\partial dp^{\tau 1}}{\partial x_j^{\tau 1}}$, $dp^{\tau 1}$, $\frac{\partial dv_{ij}^{\tau 1}}{\partial x_k^{\tau 1}}$, $dv_{ij}^{\tau 1}$ and $d\lambda_{ij}^{\tau 1}$, with $d[\cdot]^{\tau 1}$ the difference between subsequent iterative test solutions $[\cdot]^{\tau 1}$ and $[\cdot]^{\tau 2}$. The 23×23 matrix $[E^{\tau 1}]$ can be written as

$$[E^{\tau^1}] = \begin{bmatrix} E1_{(4 \times 4)}^{\tau^1} & K_{(4 \times 3)}^{WM, \tau^1} & 0_{(4 \times 8)} & 0_{(4 \times 4)} & -I_{(4 \times 4)} \\ K_{(3 \times 4)}^{MW, \tau^1} & K_{(3 \times 3)}^{WW, \tau^1} & 0_{(3 \times 8)} & 0_{(3 \times 4)} & 0_{(3 \times 4)} \\ E2_{(8 \times 4)}^{\tau^1} & 0_{(8 \times 3)} & D_{(8 \times 8)}^{\tau^1} & 0_{(4 \times 4)} & 0_{(8 \times 4)} \\ E3_{(4 \times 4)}^{\tau^1} & 0_{(4 \times 3)} & 0_{(4 \times 8)} & 0_{(4 \times 4)} & I_{(4 \times 4)} \\ E4_{(4 \times 4)}^{\tau^1} & 0_{(4 \times 3)} & 0_{(4 \times 8)} & -I_{(4 \times 4)} & 0_{(4 \times 4)} \end{bmatrix} \quad (5)$$

with $[I_{(4 \times 4)}]$ the identity matrix. Matrix $[D_{(8 \times 8)}]$ contains the relation between the double stress Σ_{ijk} and the gradient of micromechanics $\partial v_{lm}/\partial x_n$, for which a linear isotropic relation is formulated in line with the initial work of Mindlin (1965), written for the Jaumann rate of double stress $\overset{\circ}{\Sigma}$:

$$\overset{\circ}{\Sigma}_{ijk} = D_{ijklmn} \partial \dot{v}_{lm} / \partial x_n \quad (6)$$

See Bésuelle et al. (2006) or Collin et al. (2006) for the full matrix $D_{(8 \times 8)}$ representing the 6th order tensor with components D_{ijklmn} independent of the material state. The matrices $[E1]$, $[K_{WM}]$, $[K_{MW}]$ and $[K_{WW}]$ describe the relation between the classical components of the hydromechanical coupled relations. They contain both geometrical and rheological terms, the former of which can be found in Matsushima et al. (2002) and Collin et al. (2006). The rheological terms are the consistent linearizations of the constitutive relations. In the following, they will be written as follows:

$$\begin{bmatrix} C_{ijkl} & A_{ijl} & B_{ij} \\ E_{ikl} & F_{il} & G_i \\ H_{kl} & J_i & L \end{bmatrix} \begin{Bmatrix} \partial \delta u_k^M / \partial x_l \\ \partial \delta p^M / \partial x_l \\ \delta p^M \end{Bmatrix} = \begin{Bmatrix} \delta \sigma_{ij}^M \\ \delta m_i^M \\ \delta \dot{M}^M \end{Bmatrix} \quad (7)$$

or summarized as $[A_{(7 \times 7)}^{\tau^1}] \{\delta U_{(7)}^{\tau^1}\} = \{\delta S_{(7)}^{\tau^1}\}$, with $\{U_{(7)}\}$ the column vector of the 7 (in a two-dimensional problem) first order kinematical degrees of freedom ∇u^M , ∇p^M and p^M at the macroscale material point and $\{S_{(7)}\}$ their dual response terms σ^M , \dot{m}^M and \dot{M} . Spatial discretization of field Eq. (4) is done by means of 8-noded quadrilateral elements with 4 integration points, using the finite element program Lagamine (University of Liège, (Charlier, 1987)). Quadratic shape functions are used for interpolation of the displacement fields, whereas linear shape functions are used for the fluid problem. An additional 9th node is introduced at the center of the element to take into account the Lagrange multipliers λ_{ij} , which are assumed constant over the element. The reader is referred to Collin et al. (2006) for more details on the specific element used at the macroscale.

3. Microscale model for hydromechanical solid-fluid interaction

On the microscale, the microstructure of the material is defined by grains, separated by cohesive interfaces. Fluid can percolate in the pore network that is formed by these interfaces and fluid pressure acts statically on the (impermeable) grains (Figure A.2). This model was introduced by Frey et al. (2012) in large strain formulation and used to constitute a REV. The homogenized response to kinematic loading of this REV was used to provide the macroscopic material point behaviour. However, this model does not comply with the Hill-Mandel condition of macro homogeneity (Hill, 1965; Mandel, 1972), which requires the work at the microscale to be equal to the work at the macroscale.

For the consistent homogenization of the response, the microscale model by Frey et al. (2012) needed modifications to avoid non-symmetries in the stress tensors as some inconsistencies with respect to large deformations prevented the direct application of computational homogenization of the microscale model. In addition, the periodic conditions in the presence of fluid pressure gradients and the definition of a stress tensor in the interface cohe-

sive zone under large deformation required modifications of the microscale model to restore consistency. For these reasons, the following modifications were made;

- The total microscale fluid pressure in any point inside the REV is approximated by the macroscale fluid pressure p^M under the assumption of separation of scales. This assumption is required for the consistent application of fluid-to-solid interaction within the periodic frame. As a result of this, a fictitious term \hat{p} defined as $p^m = p^M + \hat{p}$ is used to capture any deviation from the macroscopic pressure as a result of both the macroscopic pressure gradient ∇p^M over the REV and the microscale spatial variation of the pore pressure as an effect of the periodic heterogeneities. More details are given in Section 3.3;
- A small strain formulation is adopted for the description of the microstructural REV. A decomposition of the macroscale deformation gradient tensor into a stretch and a rotation component is used to be able to take into account possible large rotations at the macroscale.

To couple the behaviour of the micro and the macroscale, the macroscale kinematics needs to be enforced on the REV through the boundary conditions. It is well-known that for the problems with elliptic equations underlying the REV boundary value problem (BVP), the periodic boundary conditions are the most efficient way to enforce the global kinematics on the REV (Terada et al., 2000; van der Sluis et al., 2000). Ellipticity of the equations can be lost when microscale damage or softening behaviour becomes dominant in the homogenized REV behaviour. The microscale kinematics then loses its periodicity and the homogenized response becomes dependent on the size of the REV as demonstrated by Bilbie et al. (2008) for the model under consideration.

The use of periodic boundary conditions beyond the point of loss of ellipticity leads to a material response in which the periodic frame is an inherent part of the homogenized response, first of all by defining an artificial internal length with respect to spatial repetitions of the micromechanical fracture pattern and secondly by the orientation-dependency of this internal length. Early developments of enhancement of the boundary conditions to deal with the loss of periodicity were suggested in literature, see for example (Coenen et al., 2011a; 2011b; Nguyen and Noels, 2014; Toro et al., 2014). In this work, no further enhancement is made to deal with the loss of periodicity. As a result, the periodic conditions are present in the homogenized response and as such introduce an REV size dependency in macroscopic softening behaviour. Further development of the boundary conditions, including consistency with respect to hydromechanical coupling, remains an unresolved problem.

The hydraulic problem at the microscale is formulated under steady-state conditions. Steady-state conditions are consistent with the separation of scales because the characteristic time of the fluid flow at the microscale is much smaller than the characteristic time of fluid flow at the macroscale. This assumption could be discussed if several characteristic times at the small scale would coexist, like for a double porosity model or a time dependent mechanical behavior.

3.1. Formulation of the REV periodic BVP

Two types of kinematics fields are used; those on the macroscale (u_i^M, p^M) and those on the microscale (u_i^m, p^m). The macroscale kinematics fields are considered continuous, whereas the micromechanical displacement fields u_i^m is generally discontinuous and should therefore be treated as piecewise differentiable. Discontinuities in the displacement fields are restricted to the grain interfaces, such that N continuous subdomains Ω_n can

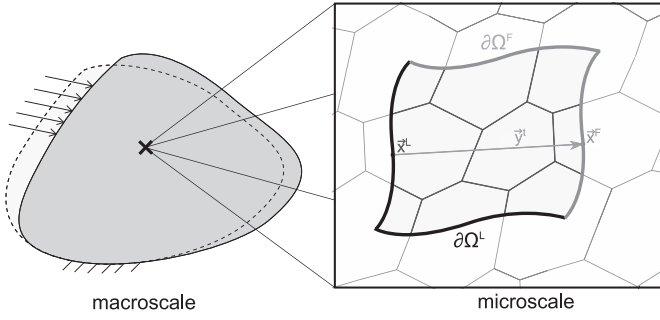


Fig. 1. Zoom on the deformed local periodic microstructure in a deformed macroscale domain. Homologous points x^L and x^F on periodic boundary segments $\partial\Omega^L$ and $\partial\Omega^F$ are as a distance of \bar{y}^L .

be identified. These subdomains are separated by interfaces, defining surface domain Γ and the boundaries of these subdomains are either the external domain boundaries $\partial\Omega$ or internal boundaries $\partial\Omega_{int}$, spatially coinciding with Γ . With these definitions, divergence theorem leads to

$$\sum_{n=1..N} \int_{\Omega_n} \frac{\partial u_i^m}{\partial x_j} dv = \int_{\partial\Omega_{int}} u_i^m n_j ds + \int_{\partial\Omega} u_i^m n_j ds \quad (8)$$

with \bar{n} the outward normal vector either to the grain boundary $\partial\Omega_{int}$ or to the REV boundary $\partial\Omega$.

Subdividing the internal boundaries into upper and lower parts of the interface walls $\partial\Omega_{int}^+$ and $\partial\Omega_{int}^-$ with corresponding displacements u_i^+ and u_i^- between which the discontinuity can be defined as $\Delta u_i = u_i^+ - u_i^-$ allows rewriting (8) into (9) with domain Γ and \bar{n} defined along $\partial\Omega_{int}^-$. Ω^c the domain of continuous solids as an assembly of the domains Ω_n and $\Omega = \Omega^c \cup \Gamma$.

$$\begin{aligned} \nabla \bar{u}^M &= \frac{1}{\Omega} \left(\int_{\Omega^c} \nabla \bar{u}^m dv + \int_{\Gamma} \Delta \bar{u}^m \otimes \bar{n} ds \right) \\ &= \frac{1}{\Omega} \int_{\partial\Omega} \bar{u}^m \otimes \bar{n} ds \end{aligned} \quad (9)$$

with n_i^- the normal outward vector of $\partial\Omega_{int}^-$ and Γ the surface domain of the grain interfaces, which is one-dimensional in the 2D computations in this work.

For microscale hydraulic pressures p^m , no discontinuities exist and the following can be written:

$$\nabla p^M = \frac{1}{\Omega} \int_{\Omega} \nabla p^m dv = \frac{1}{\Omega} \int_{\partial\Omega} p^m \bar{n} ds \quad (10)$$

In the multiscale framework, $\nabla \bar{u}^M$, ∇p^M and p^M , will be used as the macroscopic constraint on the global state of the REV and therefore are equal to $\nabla \bar{u}^M, \tau^1$, $\nabla p^M, \tau^1$ and p^M, τ^1 . These kinematic variables are part of the macroscale kinematic state vector $U^{\tau 1}$ in (4) for assessing the equilibrium of trial solution $[\cdot]^{\tau 1}$. This means that the boundary conditions will be consistent with the implicit formulation of the Newton-Raphson iterative scheme for solving the macroscale BVP of Section 2.

The coupling between the two domains is obtained by means of the assumption of local periodicity of both the microstructure and the kinematics. Homologous points on the REV boundary are found at a distance \bar{y} and periodicity of kinematics prescribes an identical behaviour of these points. Introducing lead points x^L and follow points x^F as the homologous points on opposite sides of the REV (see Fig. 1), their kinematics can be related to meet (9) and (10):

$$\bar{u}^m(x^F) = \bar{u}^m(x^L) + \nabla \bar{u}^M \cdot \bar{y} \quad (11)$$

$$p^m(x^F) = p^m(x^L) + \nabla p^M \cdot \bar{y} \quad (12)$$

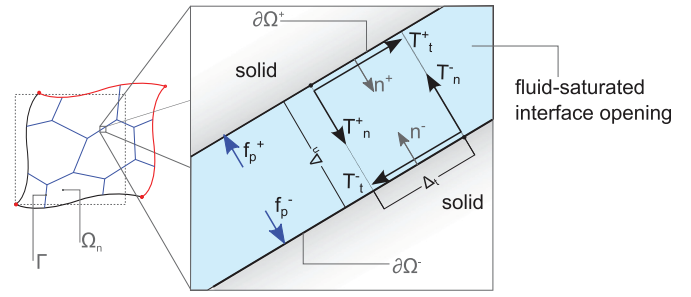


Fig. 2. microscale modelling concept.

with $\bar{n}^L = -\bar{n}^F$. This leads to

$$\nabla \bar{u}^M = \frac{1}{\Omega} \int_{\partial\Omega^F} (\nabla \bar{u}^M \cdot \bar{y}) \otimes \bar{n}^F ds \quad (13)$$

$$\nabla p^M = \frac{1}{\Omega} \int_{\partial\Omega^F} (\nabla p^M \cdot \bar{y}) \otimes \bar{n}^F ds \quad (14)$$

The periodic REV implies the continuation of the material in a repetitive way, such that a continuity of both strain (or relative displacement in case of interfaces) and stress is guaranteed. As a consequence, the REV boundary traction \bar{t} and boundary fluid fluxes $q = \bar{m} \cdot \bar{n}$ are antiperiodic, as to provide a combined equilibrium:

$$\bar{t}^F + \bar{t}^L = \bar{0} \quad (15)$$

$$q^F + q^L = 0 \quad (16)$$

The definition of the periodic conditions for hydraulic fluxes requires a steady-state assumption of the microscale problem. This assumption is in line with the separation of scales.

3.2. The microscale mechanical problem

The continuous subdomains introduced above are used to model the granular skeleton of the material. The grains are assumed to be elastic and characterized by an isotropic, linear elastic constitutive relation. Their internal balance equation ($\nabla \cdot \sigma = \bar{0}$) is solved by means of a finite element discretization using 4-node isoparametric quadrilateral finite elements, which need no further discussion. The interface between two grains is modelled by means of interface elements to take into account the cohesive traction \bar{T} acting normally and tangentially between the grains (Figure A.2). 4-node interface elements with initially zero thickness are used (see Fig. 4). Normal and tangential cohesive forces are defined independently, using a simplistic damage law dependent on parameters $T_{t/n}^{max}$ (the maximum cohesive force tangential (t) or normal (n) to the grain boundary), $0 < D_{t/n} \leq 1$ (the relative degradation of the interface) and $\delta_{t/n}^c$ (the relative interface displacement for complete degradation of the cohesive forces). Interface state parameters D_t and D_n take into account the history of the relative displacement between the opposite sides of the interface:

$$D_t^t = \max_{\tau=0..t} (D_t^0, |\Delta u_t^\tau| / \delta_t^c) \quad (17)$$

$$D_n^t = \max_{\tau=0..t} (D_n^0, \Delta u_n^\tau / \delta_n^c) \quad (18)$$

where D_t^0 and D_n^0 are two model parameters defining the state of initial degradation and thereby the initial interface stiffness. The state variables D_t^t and D_n^t at time t for the normal and tangential components individually allows writing the equations for the interface cohesion (see also Fig. 3):

$$T_t^t = T_t^{max} (1 - D_t^t) \frac{\Delta u_t^t}{D_t^t \delta_t^c} \quad (19)$$

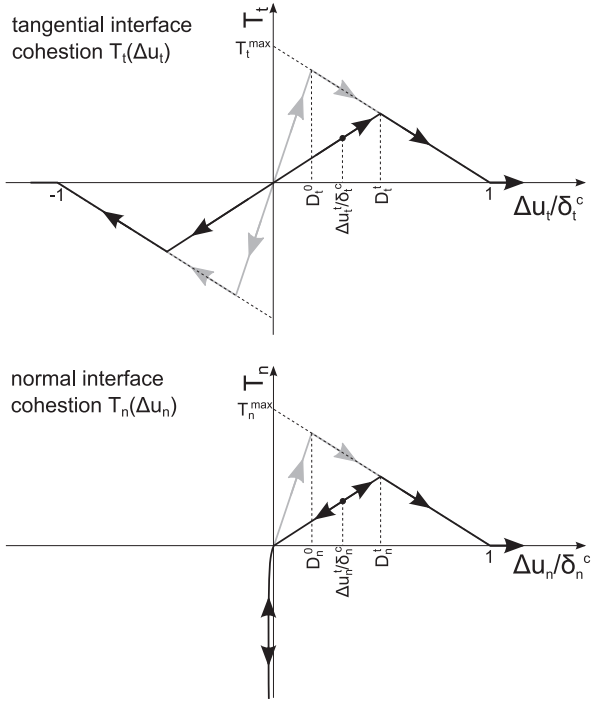


Fig. 3. Linear damage model for interface cohesion components T_t and T_n .

$$\begin{aligned}
 T_n^t &= T_n^{\max} (1 - D_n^t) \frac{\Delta u_n^t}{D_n^t \delta_n^c} & \text{if } \Delta u_n^t > 0 \\
 &= T_n^{\max} (1 - D_n^t) \frac{\Delta u_n^t}{D_n^t \delta_n^c} - \chi \Delta u_n^t{}^2 & \text{if } \Delta u_n^t < 0
 \end{aligned} \quad (20)$$

This model is equivalent to the linear softening models used for cohesive zones in for example (Geubelle and Baylor, 1998). For $D_n, D_t \rightarrow 0$ this model converges to the linear softening model by Camacho and Ortiz (1996). It should be noted that the presented model does not take into account any relation between normal and tangential components. As a result, frictional effects are not accounted for at the grain interfaces and damage can take place in each component individually. Nevertheless, mean stress dependency of strength can be found as an effect of the imbrication of the grains. This first-version model of the interface cohesive forces, consistent with formulations in Frey et al. (2012); Marinelli et al. (2016), can be changed for physically more meaningful constitutive relations without affecting the modelling framework.

The additional term $-\chi \Delta u_n^t{}^2$ for $\Delta u_n^t < 0$ is used to take into account normal contact of grains by means of penalization. The pe-

nalization term χ should be taken large to obtain physically relevant contacts with a minimum of interpenetration of grains, but not too large so to maintain the numerical accuracy of the system of equations to be solved.

Numerical integration and taking into account the fluid pressure acting normally on the grain boundaries allows deriving the element equivalent nodal forces and assembling the element stiffness matrices. This leads to the global system of equations for the mechanical part of the microscale model:

$$[K_{(n \times n)}^{mm}] \{\delta u_{(n)}\} = \{\delta f_{(n)}\} \quad (21)$$

This system of equations is used as the auxiliary system of equations $[K^{mm, \zeta^1}] \{du^{\zeta^1}\} \approx -\{df^{\zeta^1}\}$ to iteratively update the configuration $\{u^{\zeta^1}\}$ by iterative increment $\{du^{\zeta^1}\} = \{u^{\zeta^2}\} - \{u^{\zeta^1}\}$. The updated state $\{u^{\zeta^2}\}$ aims to correct for out-of-balance forces $\{df^{\zeta^1}\}$. Note that the variation of the hydraulic normal forces on the grain interfaces is not taken into account in this auxiliary system of equations. As an effect of the separation of scales, the microscale fluid pressure p^m is approximated by the macroscale fluid pressure p^M, τ^1 (see Section 3.3). This means that the hydraulics-to-mechanics coupling is enforced on the microscale in a direct way and the microscale granular configuration can be computed independent from the hydraulic problem, while maintaining the implicit formulation of the framework.

3.3. The microscale fluid problem

As introduced above, the microscale pressure is split into two parts to take into account variations in pressure gradients and variations in absolute pressure independently at the microscale:

$$p^m = p^M + \hat{p} \quad (22)$$

Under the assumption of separation of scales the two right hand terms will be of different orders of magnitude. This implies that p^M can be used for all (variations of) the total value of p^m , whereas \hat{p} can be used whenever gradients of p^m are considered, either enforced by the macroscale gradient ∇p^M or due to microstructural heterogeneity.

The pore channel network formed by the grain interfaces allows fluid to be transported as a reaction to a pressure gradient. For defining a relation between the interface configuration and the pressure gradient on one hand and the fluid mass flux on the other, the assumption on the channel shape and the type of flow is required. As the model is developed in 2D, an assumption of steady state laminar flow between smooth parallel plates is made. As a function of the fluid viscosity μ , the well-known cubic relation between fluid mass flux in the channel ϖ , the interface opening Δu_h and the pressure gradient dp/ds can be derived at a certain position s in the channel:

$$\varpi = -\rho^w \kappa(s) \frac{d\hat{p}}{ds}, \quad \kappa(s) = \frac{12}{\mu} \Delta u_h^3 \quad (23)$$

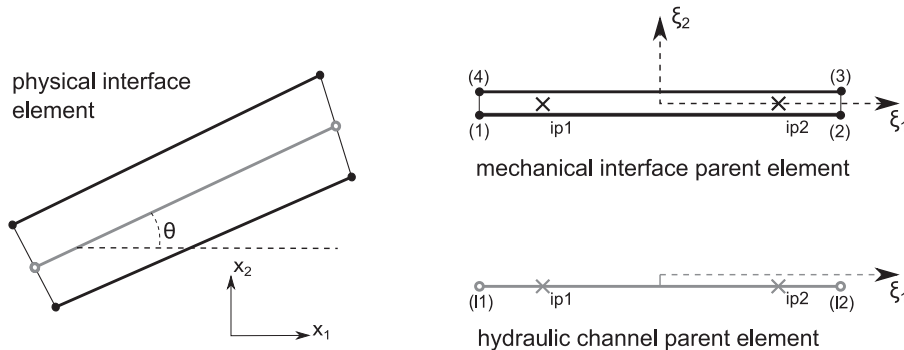


Fig. 4. Interface element with corresponding mechanical interface and hydraulic channel parent elements in local coordinate system ξ_1, ξ_2 .

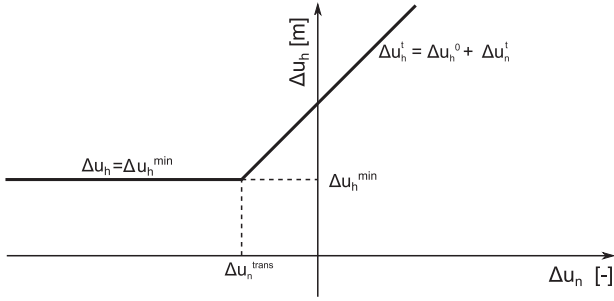


Fig. 5. Definition of the relation between normal interface opening Δu_n and hydraulic equivalent interface opening Δu_h .

The coupling term κ is here given as a function of Δu_h , which is defined by the normal opening of the interface Δu_n and contains a small correction to avoid negative-thickness or zero-thickness interface openings as this would lead to non-physical interface flow properties or numerical instabilities respectively. The translation from Δu_n to Δu_h is performed as follows:

$$\begin{aligned} \Delta u_h(s) &= \Delta u_h^{\min} - \Delta u_h^{\text{trans}} + \Delta u_n(s) & \text{if } \Delta u_n > \Delta u_h^{\text{trans}} \\ &= \Delta u_h^{\min} & \text{if } \Delta u_n \leq \Delta u_h^{\text{trans}} \end{aligned} \quad (24)$$

Two control parameters Δu_h^{\min} and $\Delta u_h^{\text{trans}}$ are introduced in this way, controlling indirectly the initial and minimum permeability of the material by guaranteeing continuous flow paths even in case of closed interfaces from a mechanical point of view (Fig. 5). The minimum permeability is a simplistic way to take into account the bulk permeability of undamaged material of low permeability, in which flow can take place through some permeable solid components. In this case, the homogenized permeability of the REV cannot be smaller than the bulk permeability of the intact material.

Fluid compressibility is taken into account, although the spatial variation of fluid density within the REV can be neglected because of the separation of scales. This means that the fluid density is a function of the macroscale pressure $p^M, \tau 1$:

$$\rho^w = \rho_0^w \exp\left(\frac{p^M}{k_w}\right) \quad (25)$$

where ρ_0^w is the fluid density at zero fluid pressure and k^w the fluid bulk modulus. With the fluid density constant over the channel and mass conservation in the channel ($d\varpi/ds = 0$) taken into account, (23) can be integrated over the length of an interface element (between $l1$ and $l2$, see Fig. 4), leading to the

$$\varpi^l = \rho^w \left(\int_{l1}^{l2} \frac{1}{\kappa(s)} ds \right)^{-1} (\hat{p}^{l2} - \hat{p}^{l1}) \quad (26)$$

the first part of the right hand side (26) is captured in a single term ϕ^l to characterize the fluid transport in channel l , containing both fluid density and channel conductivity:

$$\phi^l (\hat{p}^{l2} - \hat{p}^{l1}) = \varpi^l \quad (27)$$

With the fluid mass balance taken into account in each interface element, the domain fluid mass balance can be completed for the full domain by considering the nodal fluid mass balance q , with the nodes positioned on the intersection of interface channels. Defining the element system of equations as

$$\begin{bmatrix} q^{l1} \\ q^{l2} \end{bmatrix} = \begin{bmatrix} -\phi^l & 0 \\ 0 & \phi^l \end{bmatrix} \begin{bmatrix} \hat{p}^{l1} \\ \hat{p}^{l2} \end{bmatrix} \quad (28)$$

allows assembling the global system of equations to solve the hydraulic system of equations

$$[K_{(m \times m)}^{hh}] \{\hat{p}_{(m)}\} = \{q_{(m)}\} \quad (29)$$

where the nodal mass balance of each node i under steady state conditions requires $q_{(i)} = 0$. Enforcing the REV boundary conditions (11),(12) and (15),(16) to (29) allows solving the hydraulic system of equations directly. This gives the relative pore pressure distribution field $\hat{p}^{\tau 1}$, from which the fluid mass fluxes can be determined using the fluid density based on $p^M, \tau 1$. The microscale hydraulic system for macroscale test solution $\tau 1$ is hereby solved corresponding to microscale mechanical configuration based on $\{u^m, \tau 1\}$.

4. Computational homogenization for hydromechanical coupling

4.1. Homogenized response

Hill-Mandel principle of macro-homogeneity (Hill, 1965; Mandel, 1972) serves as the starting point of the coupling between the micro and macroscale. It states that the work performed at the macroscale is equal to the average work of the microscale:

$$W^M = \frac{1}{\Omega^{REV}} \int_{\Omega} W^m dV \quad (30)$$

With the assumption of decoupling between first and second gradient parts (Chambon et al., 2001), W^M considers the work of the first gradient part. The work of the second gradient part is accounted for by the second gradient constitutive relation (see (1)). It is straightforward to write the virtual work of the first gradient part at the macroscale corresponding to a virtual displacement field u_i^* :

$$W^M = \sigma_{ij}^M \frac{\partial u_i^M}{\partial x_j} \quad (31)$$

Given an equilibrated microscale configuration ($\nabla \cdot \sigma = 0$), with the microscale displacement field u_i^m piecewise differentiable and using the previously introduced definitions of domains and boundaries, the internal and external virtual work can be written for the subdomains as (see Section 3.1):

$$\begin{aligned} W^{*m} &= \int_{\Omega^c} \sigma_{ij}^m \frac{\partial u_i^*}{\partial x_j} d\Omega + \int_{\Gamma} (T_i - p^M n_i) \Delta u_i^{*m} ds \\ &= \int_{\partial\Omega} t_i u_i^{*m} ds \end{aligned} \quad (32)$$

$$= \int_{\partial\Omega^F} t_i \frac{\partial u_i^M}{\partial x_j} y_j ds \quad (33)$$

Note that for meeting the requirement of macro homogeneity, the small strain assumption was adopted to overcome the definition problems of stress and strain states in and around the interfaces at the microscale. For (30) to hold, this means that the macroscale stress tensor σ^M is defined as follows:

$$\sigma_{ij}^M = \frac{1}{\Omega^{REV}} \int_{\partial\Omega^F} t_i y_j ds \quad (34)$$

A similar derivative of transport problems leads to the definition of a homogenized response of microscale diffusive flow or the combination of diffusive and pore channel flow; see for example (Özdemir et al., 2008a; 2008b) for thermal flux or (Massart and Selvadurai, 2012; 2014) for fluid flux. In this work, only interface channel flow is considered, although a combination of interface channel flow and diffusive flow in the grains could be taken into account in the exact same formulation (van den Eijnden, 2015). Similar to (30) for the mechanical part of the work, the macroscale virtual work term R^{*M} related to the variation of pressure gradients has to be equal to its microscale equivalent:

$$R^{*M} = R^{*m} \quad (35)$$

with

$$R^{*M} = m_i^M \frac{\partial p^{*M}}{\partial x_i} \quad (36)$$

On the microscale, the residual of the field equations over the REV domain Ω^{REV} is expressed as:

$$R^{*m} = \frac{1}{\Omega^{REV}} \int_{\Omega^c} m_i \frac{\partial p^*}{\partial x_i} dV + \int_{\Gamma} \varpi \frac{\partial p^*}{\partial s} ds \quad (37)$$

$$= \frac{1}{\Omega^{REV}} \int_{\partial\Omega} m_i n_i p^* ds + \sum_{\partial\Gamma} \varpi p^* \quad (38)$$

where the first term on the right hand side exists in case of diffusive flow in the grains and where $\sum_{\partial\Gamma} \varpi$ the sum of the fluid flux imbalance in the interfaces, which is non-zero where interface channels join the REV boundaries. This expression can be further simplified using the antiperiodicity of the fluid fluxes:

$$R^{*m} = \frac{1}{\Omega^{REV}} \left(\int_{\partial\Omega^F} m_j n_j y_i ds + \sum_{\partial\Gamma^F} \varpi y_i \right) \frac{\partial p^{*M}}{\partial x_i} \quad (39)$$

Restriction to a microscale model with impervious grains allows defining the macroscale flux from the macro homogeneity condition as:

$$m_i^M = \frac{1}{\Omega^{REV}} \sum_{\partial\Gamma^F} \varpi y_i \quad (40)$$

Finally, the specific fluid mass M is defined using spatially constant fluid density ρ^w :

$$M = \frac{1}{\Omega} \rho^w \int_{\Gamma} \Delta u_h ds \quad (41)$$

4.2. Tangent stiffness matrix by computational homogenization

A general formulation of the variation of nodal response (δf_i , δq) to a variation of nodal kinematics (δu_i , δp) at the microscale can be formulated for the discretized microstructure, without considering the REV boundary value problem:

$$\begin{bmatrix} K_{(n \times n)}^{mm} & K_{(n \times m)}^{mh} \\ K_{(m \times n)}^{hm} & K_{(m \times m)}^{hh} \end{bmatrix} \begin{Bmatrix} \delta u_{(n)} \\ \delta p_{(m)} \end{Bmatrix} = \begin{Bmatrix} \delta f_{(n)} \\ \delta q_{(m)} \end{Bmatrix} \quad (42)$$

n and m are here the number of mechanical and hydraulic degrees of freedom respectively. Although in general, all terms in the matrices of (42) can be non-zero, it is easily verified that in the case of the micromechanical model presented above, $[K_{(n \times m)}^{mh}] = [0_{(n \times m)}]$. The matrices $[K_{(n \times n)}^{mm}]$ and $[K_{(m \times m)}^{hh}]$ are provided by the systems of equations used to solve respectively the mechanical and hydraulic microscale balance equations. Matrix $[K_{(m \times n)}^{hm}]$ contains the coupling terms, which were not required for solving the microscale field equations, but can be derived from the partial derivatives of the coupling term κ (23) from which the variation of fluid mass flux with respect to a variation of nodal positions (i.e. $\partial\kappa/\partial u_i^{node}$) is used to assemble this matrix for the coupling from mechanics to hydraulics.

To take into account the variation of the macroscopic fluid pressure p^M (which is constant while solving the microscale problem) the variation of the microscale pressure is split into two parts:

$$\delta p^m = \delta p^M + \delta \hat{p} \quad (43)$$

with δp^M the variation of the macroscale local fluid pressure and $\delta \hat{p}$ the variation due to the macroscale fluid pressure gradient (enforced by the boundary conditions of (12)) and the microkinematic fluctuation field p^f . This means that the variation δp^M and $\delta \hat{p}$ are independent.

For including the boundary conditions of the REV boundary value problem, 7 additional degrees of freedom for the macroscale boundary conditions ($\delta \nabla \bar{u}$, $\delta \nabla p$, δp) can be added to the system described in (42).

$$[K^{ext}] \begin{Bmatrix} \partial \delta u_i^M / \partial x_{j(4)} \\ \partial \delta p^M / \partial x_{j(2)} \\ \delta p_{(1)}^M \\ \delta u_{(n)} \\ \delta \hat{p}_{(m)} \end{Bmatrix} = \begin{Bmatrix} 0_{(4)} \\ 0_{(2)} \\ \delta M_{(1)} \\ \delta f_{(n)} \\ \delta q_{(m)} \end{Bmatrix} \quad (44)$$

where the extended matrix $[K^{ext}]$ has the following form:

$$\begin{bmatrix} 0_{(4 \times 4)} & 0_{(4 \times 2)} & 0_{(4 \times 1)} & 0_{(4 \times n)} & 0_{(4 \times m)} \\ 0_{(2 \times 4)} & 0_{(2 \times 2)} & 0_{(2 \times 1)} & 0_{(2 \times n)} & 0_{(2 \times m)} \\ 0_{(1 \times 4)} & 0_{(1 \times 2)} & K_{(1 \times 1)}^{MP} & K_{(1 \times n)}^{Mm} & 0_{(1 \times m)} \\ 0_{(n \times 4)} & 0_{(n \times 2)} & K_{(n \times 1)}^{mP} & K_{(n \times n)}^{mm} & 0_{(n \times m)} \\ 0_{(m \times 4)} & 0_{(m \times 2)} & K_{(m \times 1)}^{hP} & K_{(m \times n)}^{hm} & K_{(m \times m)}^{hh} \end{bmatrix} \quad (45)$$

Matrices $[K_{(1 \times 1)}^{MP}]$, and $[K_{(1 \times n)}^{Mm}]$ form the linearization of the relation between M , p^M and the microscale configuration characterized by $\{u_{(n)}\}$ around the current state, as defined in (41). As part of this linearization, $[K_{(1 \times 1)}^{MP}]$ is fully defined by the current pore volume and the derivative of (25) with respect to p^M . The boundary condition with respect to the total macroscopic pressure is hereby taken into account in (45).

The boundary conditions for $\nabla \bar{u}^M$ and ∇p^M have not yet been taken into account in this expression. To do so, the periodic boundary conditions are used to reduce the dependent degrees of freedom $\{\delta u^F\}$ and $\{\delta p^F\}$ through substitution by the periodic boundary conditions of (11) and (12). This entails a column operation in the matrix of (44), redistributing the columns related to the follow degrees of freedom over the lead degrees of freedom and the macro degrees of freedom. This means that the first 6 columns of the matrix are filled. The substitution of the follow degrees of freedom by the periodicity equations reduces the number of variables in the system of equations to $7 + n^i + m^i$, with n^i and m^i the number of mechanical and hydraulic independent (those not on the follow boundary) degrees of freedom respectively.

For the reduction of the number of equations, the equations for antiperiodic traction (15) and (16) are used to evaluate the combined nodal balance of the degrees of freedom on homologous nodes. At the same time, the equations of the homogenized response (34) and (40) are used to provide the dual terms for the variation of strain and pressure gradient in the upper six equations. The result is a reduced system of equations with independent mechanical and hydraulic degrees of freedom:

$$\begin{bmatrix} K_{(7 \times 7)}^{*MM} & K_{(7 \times 7)}^{*Mm} & K_{(7 \times 7)}^{*Mh} \\ K_{(n^i \times 7)}^{*mM} & K_{(n^i \times n^i)}^{*mm} & 0_{(n^i \times m^i)} \\ K_{(m^i \times 7)}^{*hM} & K_{(m^i \times n^i)}^{*hm} & K_{(m^i \times m^i)}^{*hh} \end{bmatrix} \begin{Bmatrix} \delta U_{(7)} \\ \delta u_{(n^i)} \\ \delta \hat{p}_{(m^i)} \end{Bmatrix} = \begin{Bmatrix} \delta S_{(7)} \\ \delta f_{(n^i)}^* \\ \delta q_{(m^i)}^* \end{Bmatrix} \quad (46)$$

with

$$\{\delta U_{(7)}\} = \begin{Bmatrix} \frac{\partial \delta u_1^M}{\partial x_1} \\ \frac{\partial \delta u_1^M}{\partial x_2} \\ \frac{\partial \delta u_2^M}{\partial x_1} \\ \frac{\partial \delta u_2^M}{\partial x_2} \\ \frac{\partial \delta p^M}{\partial x_1} \\ \frac{\partial \delta p^M}{\partial x_2} \\ \delta p^M \end{Bmatrix} \quad (47)$$

and

$$\{\delta S_{(7)}\} = \begin{Bmatrix} \delta \sigma_{11} \\ \delta \sigma_{12} \\ \delta \sigma_{21} \\ \delta \sigma_{22} \\ \delta m_1 \\ \delta m_2 \\ \delta M \end{Bmatrix} \quad (48)$$

As the system of equations is build for an equilibrated configuration of the microstructure, the nodal residuals f_i^* and q^* are approximately zero. These nodal residuals include the combined nodal balance of homologous points. This allows to condense the system of equations in (46) by static condensation on the remaining 7 macro degrees of freedom:

$$[A^*]\{\delta U\} = \{\delta S\} \quad (49)$$

with

$$[A^*] = [K^{*MM}] - [K^{*Mm} \quad K^{*Mh}] \begin{bmatrix} K^{*mm} & 0 \\ K^{*hm} & K^{*hh} \end{bmatrix}^{-1} \times \begin{bmatrix} K^{*mM} \\ K^{*hM} \end{bmatrix} \quad (50)$$

A final transformation is needed to change from a formulation of $[A^*]$ for variation of fluid mass δM to a formulation $[A]$ for variation of the rate of change of the fluid mass $\delta \dot{M}$. For the incremental time step Δt in the macroscale BVP, \dot{M} is computed as

$$\dot{M}^t = \frac{M^t - M^{t-\Delta t}}{\Delta t} \quad (51)$$

This leads to the expression of $\delta \dot{M}$

$$\delta \dot{M} = \frac{\delta M^t}{\Delta t} \quad (52)$$

The transformation of $[A^*]$ into $[A]$ therefore comprises dividing the seventh row of $[A^*]$ by Δt . As a result, matrix $[A]$ contains all tangent operator terms in (7) and thereby fully characterizes the classical part of the constitutive relations for the poromechanical continuum presented in Section 2. In this form, the classical part of the constitutive relations shows similarities with the formulation of Biot theory. Section 5.5 contains a further discussion on this topic.

The microscale routine for deriving the macroscopic response and consistent tangent operators for a given macroscale configuration as presented above is summarized in Fig. 6.

4.3. Small stretch / large rotation

In order to meet the requirements of the continuity of stress at the microscale, which is compromised by the cohesive zone models at the grain interfaces in case of large deformations, a small

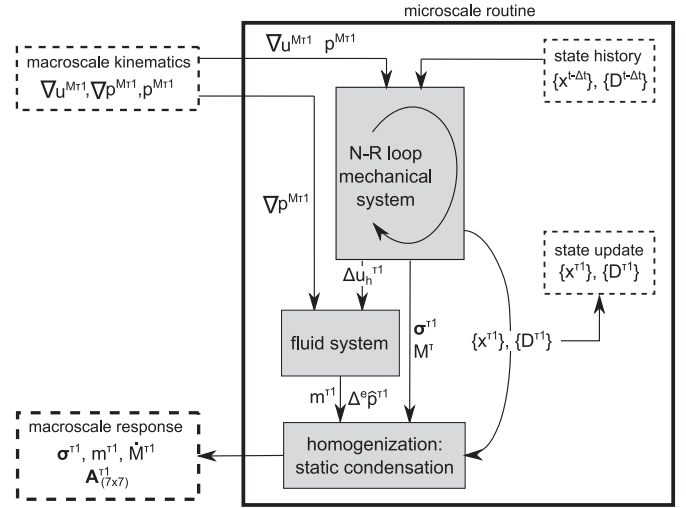


Fig. 6. Schematic representation of microstructure routine for solving the REV BVP and deriving the consistent tangent operators for the local kinematics of a macroscale trial Ω^{r2} to solution Ω^r . Passing of some microscale internal variables (global systems of equations,...) not shown. After (van den Eijnden, 2015).

strain assumption is used on the microscale. To meet the large strain formulation of the macroscale as well as possible, the principle of frame-invariance is used to be able to take into account possible large macro rotations. This is done by decomposing the macroscale deformation gradient tensor F^M into a rotational component R and a symmetric stretch component U :

$$F_{ij}^M = R_{ik}^M U_{kj}^{REV} \quad (53)$$

The rotation is equally applied to the transition of the macroscale pressure gradient:

$$\nabla_i^M p = R_{ij}^M \nabla_j^{REV} p \quad (54)$$

Macroscale stretch tensor U^{REV} (assumed approximately identical to the identity matrix) and $\nabla^{REV} p$ are used for describing the boundary conditions of the REV ((11) and (12)), after which the homogenized response is rotated back to the macroscale using rotation tensor R^M . The back-rotation in the upscaling is applied on both REV stress response σ^{REV} and fluid mass flux response \bar{m}^{REV} :

$$\sigma_{ij}^M = R_{ik}^M \sigma_{kl}^{REV} R_{jl}^M \quad (55)$$

$$m_i^M = R_{ij}^M m_j^{REV} \quad (56)$$

The rotation of the consistent tangent stiffness matrices are not frame-objective and require a more extensive operations, which can be found in Appendix A. This procedure can be considered as a separate operation between the macro and microscale and will not be mentioned explicitly hereafter.

5. Application in doublescale modelling of biaxial compression tests

5.1. Microstructure modelling

Based on Voronoi tessellation of random periodically repeated sites, a periodic microstructure is generated (Fritzen et al., 2009).

Voronoi diagrams were proposed to represent brittle rocks such as granite (Massart and Selvadurai, 2012), shale (Yao et al., 2016), marble (Alonso-Marroquín et al., 2005) and also clay rock (van den Eijnden, 2015), although the Voronoi diagram does not always match the geometry of the microstructural pattern perfectly. The

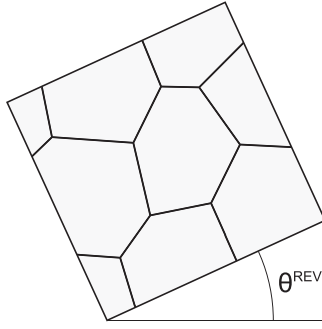


Fig. 7. Definition of the angle of REV rotation θ^{REV} to control the orientation of the microstructure with respect to the macroscale domain.

main objective of generating the microstructure from Voronoi diagrams is to have user-objective realizations of unstructured grain assemblies, versatile enough to control the orientation distribution. In future applications, Voronoi tessellation can be replaced by more advanced algorithms to reproduce the specific material microstructure under consideration, see for example (Sonon et al., 2012).

By stretching and rotating the distance functions of the tessellation, a bedding can be simulated through the grain shape with parameters β^{bed} for the orientation of the bedding plane with respect to the horizontal and ξ for the average elongation index of the individual grains. In addition, a shape correction is applied to avoid Voronoi diagrams with very short grain boundary sections. This correction is based on the optimization of the position of vertices that form the connections of the grain boundary sections with respect to the minimum of the sum of the diagram section lengths. Given the set of N section lengths l^n with $n = 1..N$, defined by M vertices with coordinates x_i^m and $m = 1..M$, the quadratic sum L of diagram sections is defined;

$$L = \sum_{n=1}^N (l^n)^2 \quad (57)$$

The coordinates of the vertices corresponding to a minimum of L (referred to as \bar{x}^{min}) are solved for to smoothen the shape of the grains and allow a better spatial discretization by means of finite elements. This minimum is found by solving the $2M$ equations:

$$\frac{\partial L}{\partial x_i^m} = 0 \quad (58)$$

Once the optimized solution \bar{x}^{min} is found, a linear combination between the original Voronoi vertices \bar{x}^0 and the optimized vertices \bar{x}^{min} is taken by means of a parameter $0 \leq \eta \leq 1$:

$$\bar{x}_n^{vertex} = (1 - \eta)\bar{x}_n^0 + \eta\bar{x}_n^{min} \quad (59)$$

A rotation angle θ^{REV} is introduced to define the orientation of the REV with respect to the macroscale sample (see Fig. 7). This rotation allows studying the structural response of samples with different orientations of the anisotropy, which itself is a material property inherently linked to the microstructure under consideration.

The representativeness of the microstructure is an argument for a high number of grains to be taken into account in the REV, in line with the classical definition of the REV. Arguments for smaller REV's come from the computational load that comes with the evaluation of larger REV's; the time required for solving the microscale BVP scales quadratically with the number of degrees of freedom in its discretization. This requires a compromise between representativeness of the REV and the computational load to be accepted. However, localized damage patterns that develop in the softening

Table 1

Microscale constitutive properties for the microstructural REV in Fig. 8.

Microscale solid constitutive parameters			
μ	= 3.00 GPa	λ	= 2.00 GPa
Microscale interface constitutive parameters			
T_n^{max}	= 5.00 MPa	T_n^{max}	= 2.00 MPa
δ_n^c	= 0.05 mm	δ_n^c	= 0.05 mm
D_n^0	= 0.01	D_n^0	= 0.01
Δu_h^{trans}	= -0.02 μm	Δu_h^{min}	= 0.02 μm
Grain geometry parameters			
ξ	= 1.67	β^{bed}	= 0°
η	= 0.20		

regime can introduce a specific number of localization paths per REV, the spacing of which is in direct relation with the choice of the number of grains. Therefore, this choice influences the softening response of the REV. In a first attempt, a relatively simple REV with 16 grains is used and no attempt is made to determine its representativeness. The influence on the softening response is thereby considered as part of the constitutive behaviour.

The stiffness of the grains is homogeneous over the REV with Lamé parameters $\mu = 3.0$ GPa and $\lambda = 2.0$ GPa. Identical parameters are used for the normal and tangential components of the interface cohesion and all interfaces have the same cohesive relations. This means that any anisotropy in the macroscale response is due to the geometry of the microstructure and the orientation of the boundary conditions rather than a phenomenological expression in the microscale constitutive relations. A horizontal elongation of 67% (i.e. $\xi = 1.67$ and $\beta^{bed} = 0^\circ$). Grain shape correction is applied with $\eta = 0.20$ to avoid a highly irregular distribution of grain boundary section lengths. For guaranteeing a well-posed hydraulic system of equations and a minimum permeability of the material, the coupling between the interface hydraulic opening is characterized by $\Delta u_h^{min} = 2 \times 10^{-5}$ mm and $\Delta u_h^{trans} = -2 \times 10^{-5}$ mm according to (24). For the given microstructure at $\theta^{REV} = 0^\circ$, this corresponds to the following initial permeability tensor;

$$\mathbf{k}^0 = \begin{bmatrix} 2.652 & 0.062 \\ 0.062 & 1.233 \end{bmatrix} \times 10^{-20} \text{ m}^2 \quad (60)$$

The parameters for used to characterize the microscale components of the material are summarized in Table 1.

5.2. Macroscale configuration and boundary conditions

A biaxial compression test of a fully saturated sample of dimensions 38×76 mm is simulated. Drainage is applied on the top and the bottom of the sample, the sample sides are impervious. A deformation-controlled loading rate of $\dot{\epsilon}_a = 1 \times 10^{-8} \text{ s}^{-1}$ is applied, which for the initial permeability of the material corresponds to transient conditions. The sample ends are considered to be perfectly smooth to simulate a biaxial compression test without friction between the end platens and the sample (see Fig. 8). No lateral confinement is applied and the initial total stress and fluid pressure are zero. The macroscale domain is discretized by a regular mesh of 10×20 square quadrilateral elements. Defects are introduced on the macroscale mesh by reducing the maximum cohesion terms T_n^{max} and T_t^{max} by 5% for the microstructures in elements of the lower left and right corners. As there is no uniqueness of solution when strain localization starts (Bésuelle et al., 2006; Chambon and Moullet, 2004), the weakened elements constitute an attractor towards one of the possible localized solutions. Defects in both lower corners has been preferred to a single defect in one of the lower corners, to keep the symmetry with respect

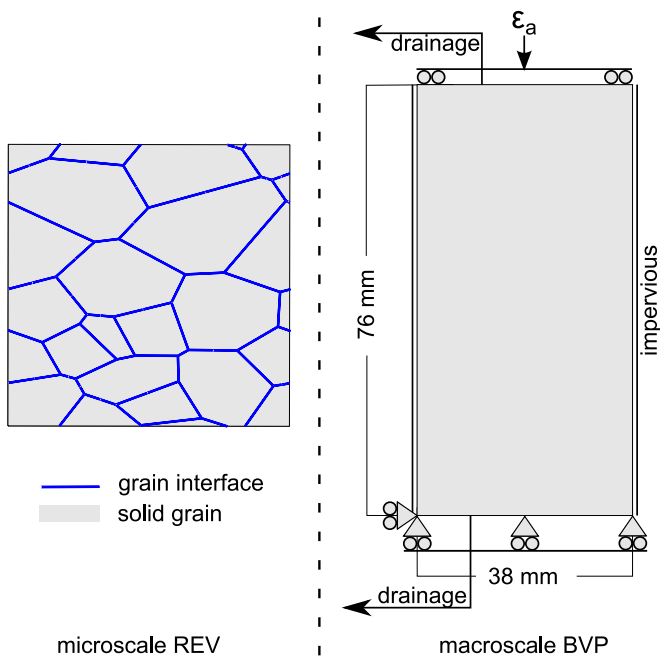


Fig. 8. Left: 16-grain microstructural REV with grain shape anisotropy $\xi = 1.67$ and bedding orientation $\beta^{bed} = 0^\circ$. Right: macroscale configuration and boundary conditions.

to the vertical axis of the specimen; the material anisotropy itself introduces a dissymmetry of the specimen and is expected to be influenced by either one of the two defects.

5.3. Mesh objectivity and second gradient model calibration

Regularization of the solution is through the local second gradient model for poromechanical problems (Collin et al., 2006), providing mesh-objective solutions. As a special case of the more general form initially introduced by Mindlin (1964), sixth-order tensor \mathbf{D} in (6) is here fully characterized by a linear elasticity parameter D [N]. This parameter implicitly scales the width w of the shear band as $w \propto \sqrt{D/\bar{C}}$, where \bar{C} is the determinant of the acoustic tensor and therefore depends on the first gradient operator \mathbf{C} in (7) and the orientation of the band (Bésuelle et al., 2006; Chambon et al., 1998; Kotronis et al., 2008). With an evolving and anisotropic first gradient operator \mathbf{C} , the width of the localization band and the effectiveness of regularization is difficult to predict accurately. The parameter D is therefore determined iteratively in a series of calibration computations. As a result of this, $D = 1.0$ kN is found to give mesh-objective results in case of strain localization for the mesh density used in the examples below.

It has to be emphasized that the local second gradient model is here deployed purely as a regularization technique and the double stress does not represent the microstructural effects in the way it does in the formalism of micromorphic continua. In analogy with this, the width of the macroscale shear bands has no physical connection with the microstructural length scales. Note that the constitutive parameters could be adjusted to reproduce the true band thickness of the material (El Moustapha, 2014). However, the bands can be very thin with respect to the size of the problem and would need some very thin elements, increasing dramatically the number of elements. As a result of the phenomenological formulation of the second gradient model, the macroscale shear band has to be seen as a continuous, homogenized representation of a localization of micro-cracks or a fault.

To demonstrate the mesh objective results obtained through regularization by the second gradient model, a series of biaxial compression tests is performed. This series corresponds to the BVP introduced in Fig. 8 for microstructure orientation $\theta^{REV} = 60^\circ$. In addition to the 10×20 reference mesh in later computations, a coarser mesh (5×10 elements), a finer mesh (20×40 elements) and an unstructured mesh (247 elements) are used. The deformed mesh with the corresponding VM equivalent strain fields are presented in Fig. 9(b), (a), (e) and (c) respectively. The white lines indicate the cross-section of the shear band as it developed in the 10×20 mesh. Length and position of the line are kept the same for the four subfigures to properly compare the width and location of the shear bands in the different meshes. It can be concluded that from the consistent width of the shear band and the general agreement of strain localization patterns, the model is mesh objective at least for the 10×20 and 20×40 meshes. The 5×10 mesh in 9(a) shows a small deviation from the other meshes and might suffer from some minor mesh dependency, particularly around the reflection of the shear band at the lower sample boundary. Some artifacts from extrapolation and smoothing in plotting the strain field are visible in 9(c). Nevertheless, the general pattern of strain localization is consistent between the four meshes with equal parameters D , demonstrating the mesh-objectivity of the model.

Fig. 9(d) and (f) show the deformed meshes of computations with parameter $D = 250$ N and $D = 4000$ kN respectively. Comparison with the deformed meshes for $D = 1000$ N demonstrates the relation between parameter D and the length scale of macroscale response (the width of the shear bands). To facilitate a more fair comparison of the shear bands, deformed meshes are shown for different levels of nominal axial strain but approximately equal state of local deformation inside the shear bands. For $D = 250$ N in 9(d) this means a nominal axial strain of $\varepsilon_a \approx 0.4\%$, whereas the nominal axial strain in 9(f) reaches $\varepsilon_a = 0.7\%$. With the width of the bands in 9(d) and (f) being respectively two times as small and two times as large as width of the shearband in 9(e), the relation between D and shearband width w is demonstrated at least in an approximated way.

5.4. Simulation results

Simulations are conducted with different orientations of the microstructure by means of different REV orientations θ^{REV} . Fig. 10 shows the global reaction force to deformation loading in four of such simulations. The responses for different values of θ^{REV} show orientation-dependency of the initial material stiffness, the material strength (peak response) and the softening behaviour.

Fig. 11 contains the deformed meshes at the macroscale with Von Mises equivalent (VM) strains and relative fluid fluxes, together with a deformed microstructural REV corresponding to an integration point inside the zone of localized strain. The deformation pattern at the macroscale shows localization of the deformation in shear bands.

Inspection of the fluid flux field as the response to the biaxial compression shows the general trend of fluid transport towards the active localization bands. This behaviour is in line with the positive pore volume rate due to the separation of the grains at the interfaces. This causes an under pressure and therefore an influx of pore fluid in the zones of localized.

The lower part of Fig. 11 shows the deformed microstructures of an integration point inside the shear band of each of the simulations, indicated in the deformed mesh by the points A. It is important to observe here that the orientations of the patterns of interface softening at the microscale do not necessarily align with the shear bands at the macroscale.

To demonstrate the coupling between the deformation and the fluid transport properties, a point that shows strong evolution of

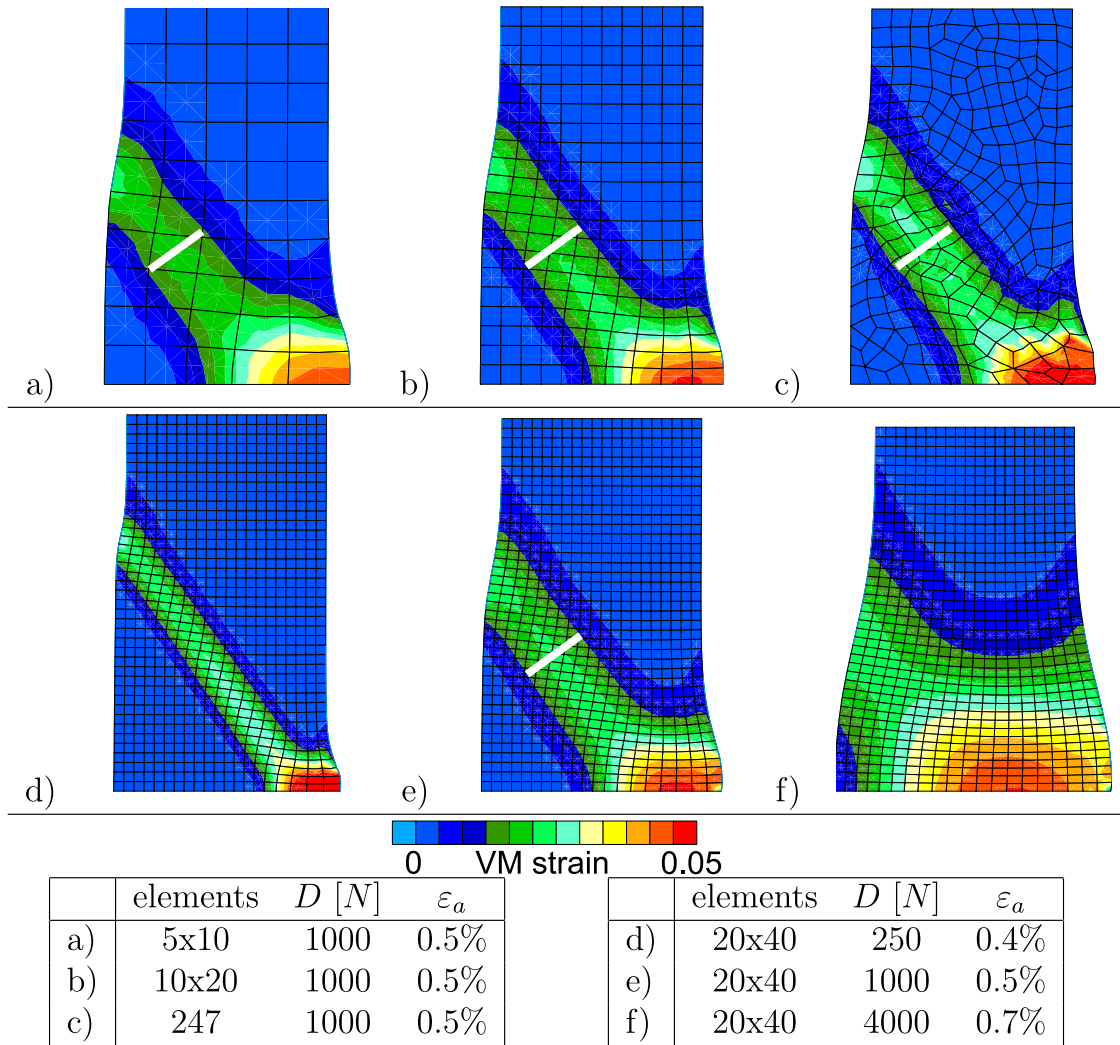


Fig. 9. Deformed domains at $\varepsilon_a = 0.5\%$ for different mesh densities (a) and different second gradient parameters D (b). Displacements multiplied $\times 10$.

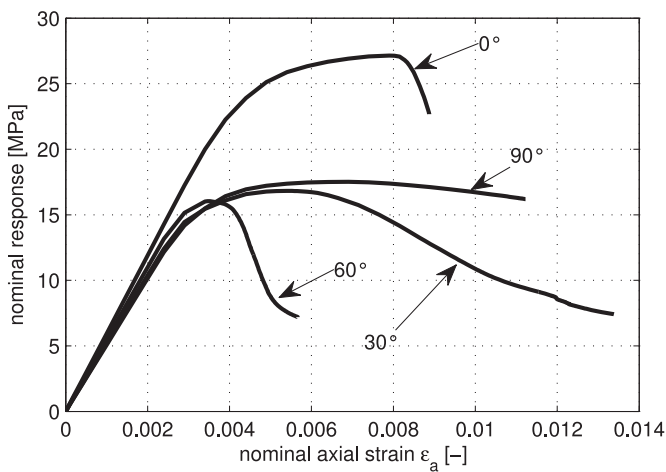


Fig. 10. Nominal stress response to unconfined biaxial compression for different microstructural REV orientations.

permeability is investigated during the simulation with $\theta^{REV} = 30^\circ$ (Point C in Fig. 11). A reference point far away from the zone of localized deformation is studied as a reference point (Point D in Fig. 11). The deformed microstructures for these points at the end

of the simulations are given in Fig. 12. They show a different mode of deformation than observed at point A in Fig. 11 because different loading paths are followed as soon as the homogeneous deformation of the sample is lost; a more continuous network of opened interfaces has developed in point C, leading locally to a significant increase in permeability (2 orders of magnitude). The principal components of the permeability tensor k_1 and k_2 for points C and D are followed during the simulation and their evolutions are given in Fig. 13. It can be observed that the evolution at points C and D are identical until $\varepsilon_a \approx -0.006$, at which a softening response starts (see Fig. 10). At higher states of axial shortening of the sample, the localized deformation forms zones with strongly increasing permeability (point C), as more continuous fluid percolation paths appear with the opening of interfaces. However, due to the two-dimensionality of the model, the evolution of permeability is restricted compared to three dimensional model, as the required contacts between grains under compressive loading prevents the development of fully continuous flow paths.

5.5. Closing remarks

The macroscale formulation in Section 2 is the formulation of a general poromechanical continuum under saturated conditions. Therefore a comparison with the formulation of Biot theory can be made. Marinelli et al. (2016) modelled oedometric compression

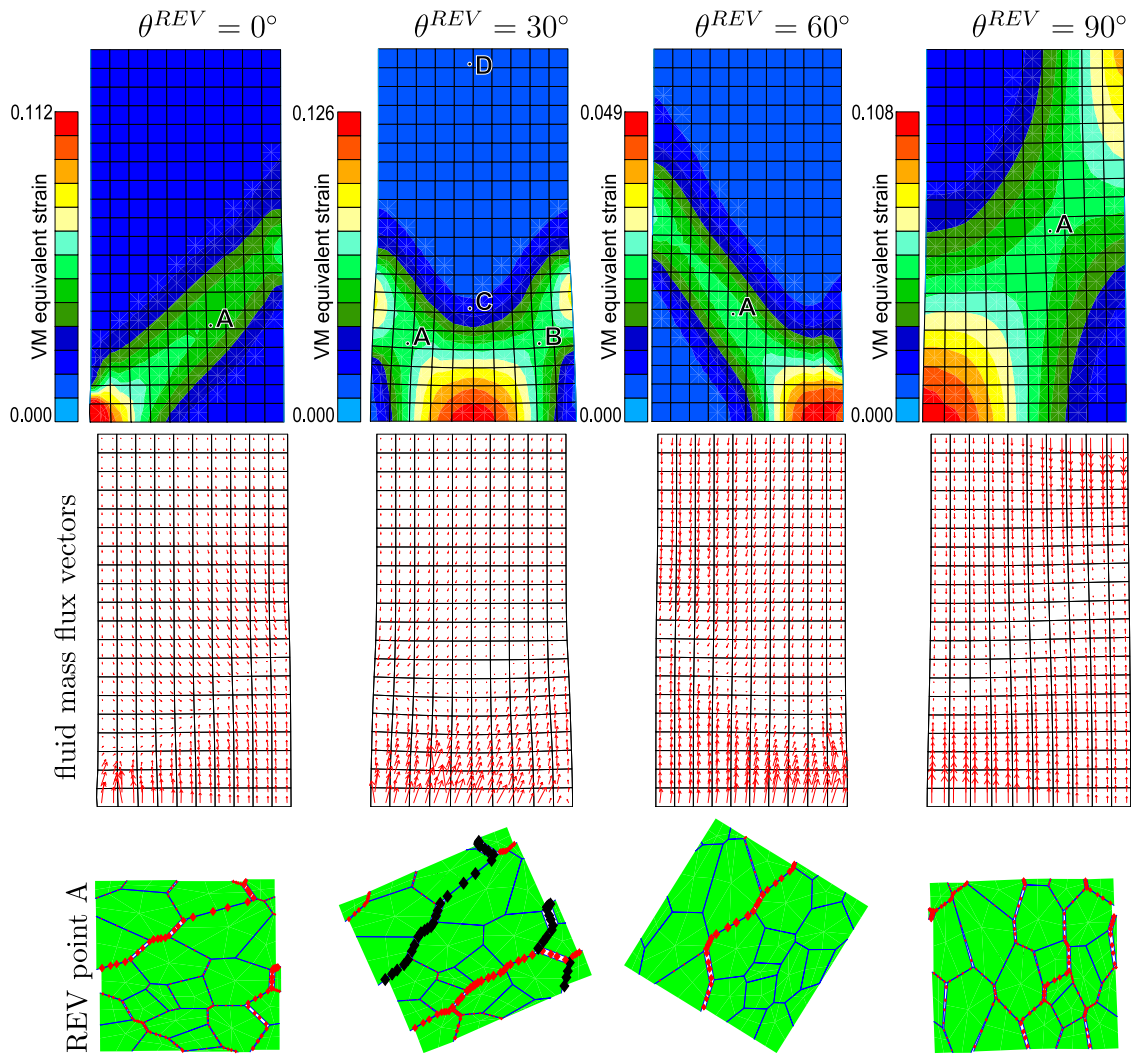


Fig. 11. Deformed microstructure and fluid mass fluxes at $\varepsilon_a = 0.015$ for $\theta^{REV} = 90^\circ$ and $\dot{\varepsilon}_a = 1 \times 10^{-8}$. Deformed microstructures in the zones of localized deformation for biaxial compression tests at different REV orientations θ^{REV} . Symbols \blacklozenge and \blacklozenge represent the interface state in softening ($D^0 < D^f < 1$) and decohesion ($D^f = 1$) respectively. Symbol size is relative to D^f .

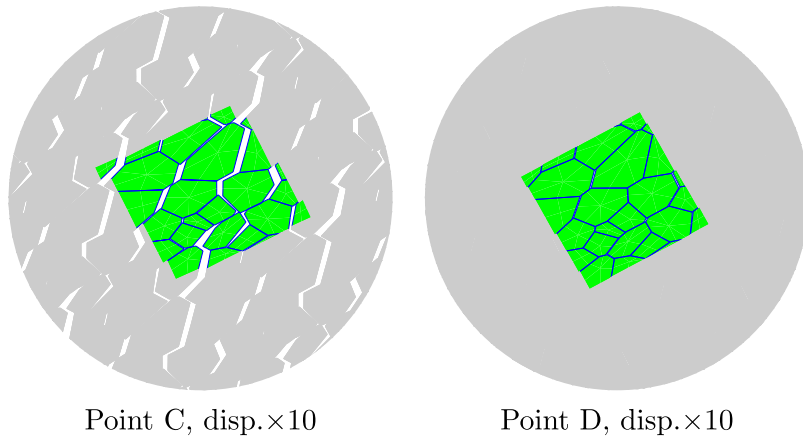


Fig. 12. Deformed microstructures at the end of the simulation for points C and D, indicating the preferential directions of permeability dictated by the continuous flow paths between the grains.

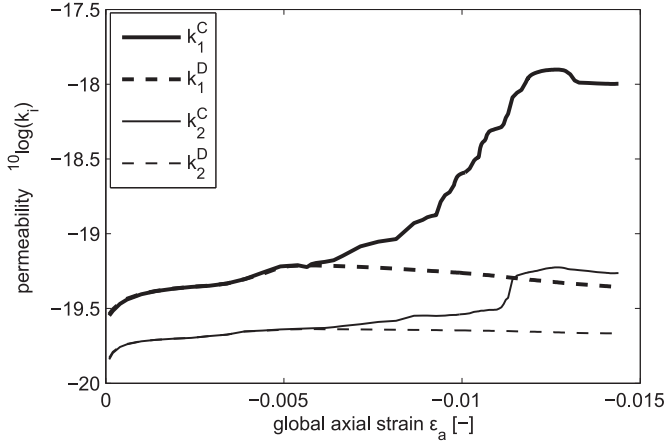


Fig. 13. Evolution of the principal components of the permeability tensor k_1 and k_2 at points C and D in the $\theta = 30^\circ$ biaxial test.

tests under poroelastic conditions with an adapted version of the model by Frey et al. (2012). The comparison with the analytical solution of the Biot theory demonstrates that the model is capable of reproducing consolidation processes. Although a different homogenization approach was used, the same tangent operators as given in (7) were derived in Marinelli et al. (2016) to make a comparison with Biot coefficients (Biot, 1941). Biot coefficient b is demonstrated to be strongly influenced by the relative stiffness of the interfaces with respect to the grain stiffness. As a result, b tends to be close to 1 in most cases of microstructure characterization. This value decreases with an increasing stiffness of the interface relative to the grains. Also, anisotropy and the dependency of the current state of the microstructure are present in the homogenized response. This leads to deviations from the classical Biot theory, in which parameters are generally constant and isotropic. With the given examples in this work and the results of Marinelli et al. (2016) it can be concluded that the model can be applied in the simulation of granular solids and capture consolidation processes at least for values b close to 1.

In the given examples, dimensions of the REV were not specified explicitly. This is consistent with the doublescale framework from a mechanical point of view since all microstructure dimensions can be expressed relative to the REV. This means that the mechanical part of the model can be applied independent from the grain size. However, the translation from interface openings to hydraulic conductivity (Eqs. (23),(24)) defines a hydraulic interface opening relative to the fluid viscosity, which introduces a length scale in the formulation of the hydraulic system. This indirectly introduces REV dimensions. In the presented examples, the REV dimensions were defined as $1 \text{ mm} \times 1 \text{ mm}$. Although the validity of the separation of scales in this example could be argued, the only point in which the definition of the REV size has a significant influence, apart from the conceptual consistency, is in the (evolution of) the permeability. In case of future applications in which dimensions of grain size and interface cohesion parameters are both defined in an absolute sense, the dimensions of the REV have to be defined explicitly and the separation of scales has to be verified for conceptual consistency of the modelling approach.

The computation time for the presented doublescale examples is mainly determined by the total loading steps required for applying the desired loading path. With the computation time for a single macroscale iteration in the order of 1 min, the total computation time for the presented simulations, performed with a single CPU, was between 10 h and 1 day as many small loading steps were required to obtain proper convergence of the NR iterative scheme in the post-peak domain.

6. Conclusions

In this paper a FE² approach for the modelling of hydromechanical coupling was presented. The behaviour of a poromechanical continuum at the macroscale is derived from the modelling of the underlying interaction between a solid granular microstructure and the pore fluid. The extension of the framework of computational homogenization to hydromechanical coupling was derived from the macro homogeneity condition for the work of the first gradient part of the model. For the modelling of softening behaviour, the multiscale model was combined with a local second gradient paradigm to avoid the well-known mesh dependency of the classical finite element while maintaining decoupled from the (local) constitutive relations of the first gradient part.

The application of the doublescale model for hydromechanical coupling in combination with a local second gradient model is demonstrated to be suitable for the modelling of localization problems with hydromechanical coupling in a transient domain. The results are a good perspective on obtaining a general way of modelling material anisotropy, hydromechanical coupling and a full history dependency, based on simple micromechanical constitutive relations with consideration of the material microstructure.

Acknowledgments

The first author thanks the French national radioactive waste management agency (Andra) for financial support. Denis Caillerie is thanked for his contribution to Section 3. The laboratory 3SR is part of the LabEx Tec 21 (Investissements d'Avenir - grant agreement n°ANR-11-LABX-0030).

Appendix A. Rotation of the consistent tangent operators

The 7×7 consistent tangent operator introduced in (7) is repeated here without reference to coordinate system $[]^M$ or $[]^{REV}$.

$$\begin{bmatrix} C_{ijkl} & A_{ijl} & B_{ij} \\ E_{ikl} & F_{il} & G_i \\ H_{kl} & J_i & L \end{bmatrix} \begin{Bmatrix} \partial \delta u_k / \partial x_l \\ \partial \delta p / \partial x_l \\ \delta p \end{Bmatrix} = \begin{Bmatrix} \delta \sigma_{ij} \\ \delta m_i \\ \delta \dot{M} \end{Bmatrix} \quad (\text{A.1})$$

The computational homogenization delivers the tangent operators in $[]^{REV}$ although the macroscale computation requires all tangent operators in $[]^M$. The objective rotation from configuration $[]^{REV}$ to $[]^M$ related to the decomposition of the macroscale deformation gradient tensor \mathbf{F} into stretch \mathbf{U} and rotation \mathbf{R} demands the following operations for the different parts of the tangent operator:

$$\begin{aligned} C_{ijkl}^M &= R_{i\alpha} R_{j\beta} C_{\alpha\beta\gamma\delta}^{REV} \frac{\partial U_{\gamma\delta}}{\partial F_{kl}} \\ &+ \frac{\partial R_{i\alpha}}{\partial F_{kl}} \sigma_{\alpha\beta}^{REV} R_{j\beta} + R_{i\alpha} \sigma_{\alpha\beta}^{REV} \frac{\partial R_{j\beta}}{\partial F_{kl}}^M \end{aligned} \quad (\text{A.2})$$

$$A_{ijk}^M = R_{i\alpha} R_{j\beta} R_{k\gamma} A_{\alpha\beta\gamma}^{REV} \quad (\text{A.3})$$

$$B_{ij}^M = R_{i\alpha} B_{\alpha\beta}^{REV} R_{j\beta} \quad (\text{A.4})$$

$$E_{ikl}^M = m_{\alpha}^{REV} \frac{\partial R_{\alpha i}}{\partial F_{kl}} + R_{i\alpha} E_{\alpha\gamma\delta} \frac{\partial U_{\gamma\delta}}{\partial F_{kl}} \quad (\text{A.5})$$

$$F_{il}^M = R_{i\alpha} R_{l\gamma} F_{\alpha\gamma}^{REV} \quad (\text{A.6})$$

$$G_i^M = R_{i\alpha} G_{\alpha}^{REV} \quad (\text{A.7})$$

$$H_{kl}^M = H_{\gamma\delta}^{REV} \frac{\partial U_{\gamma\delta}}{\partial F_{kl}} \quad (\text{A.8})$$

$$J_l^M = R_{l\delta} J_{\delta}^{REV} \quad (\text{A.9})$$

$$L^M = L^{REV} \quad (\text{A.10})$$

with:

$$\begin{aligned} \frac{\partial U_{\gamma\delta}}{\partial F_{kl}^M} &= \frac{1}{I_1} \frac{\partial R_{kl}}{\partial \theta} ((\delta_{\gamma 2} - \delta_{\gamma 1}) \delta_{\gamma\delta} U_{12}) + \delta_{\gamma 1} \delta_{\delta 1} R_{kl} \\ &+ \frac{1}{I_1} \frac{\partial R_{kl}}{\partial \theta} ((1 - \delta_{\gamma\delta})(\delta_{l2} U_{11} - \delta_{l1} U_{22})) \end{aligned} \quad (\text{A.11})$$

and

$$\frac{\partial R_{i\alpha}}{\partial F_{kl}} = \frac{1}{I_1} \frac{\partial R_{i\alpha}}{\partial \theta} \frac{\partial R_{kl}}{\partial \theta} \quad (\text{A.12})$$

where I_1 is the first strain invariant $tr(\mathbf{U})$, δ_{ij} is the Kronecker delta and θ is the angle of rotation represented by \mathbf{R} .

References

- Aifantis, E., 1984. On the microstructural origin of certain inelastic models. *ASME. J. Eng. Mater. Technol.* 106(4), 326–330.
- Alonso-Marroquín, F., Luding, S., Herrmann, H.J., Vardoulakis, I., 2005. Role of anisotropy in the elastoplastic response of a polygonal packing. *Phys. Rev. E* 71, 051304.
- Bésuelle, P., Chambon, R., Collin, F., 2006. Switching deformation modes in post-localization solutions with a quasibrittle material. *J. Mech. Mat. Str.* 1, 1115–1134.
- Bilbie, G., Dascalu, C., Chambon, R., Caillerie, D., 2008. Micro-fracture instabilities in granular solids. *Acta Geotechnica* 3 (1), 25–35.
- Biot, M., 1941. General theory of three-dimensional consolidation. *J. Appl. Phys.* 12 (2), 155–164.
- Camacho, G., Ortiz, M., 1996. Computational modelling of impact damage in brittle materials. *Int. J. Solids Struct.* 33 (20–22), 2899–2938.
- Chambon, R., Caillerie, D., 1999. Existence and uniqueness theorems for boundary value problems involving incrementally non linear models. *Int. J. Solids Struct.* 36 (33), 5089–5099.
- Chambon, R., Caillerie, D., Hassan, N.E., 1998. One-dimensional localisation studied with a second grade model. *Eur. J. Mech. - A/Solids* 17 (4), 637–656.
- Chambon, R., Caillerie, D., Matsushima, T., 2001. Plastic continuum with microstructure, local second gradient theories for geomaterials: localization studies. *Int. J. Solids Struct.* 38 (46–47), 8503–8527.
- Chambon, R., Moullet, J., 2004. Uniqueness studies in boundary value problems involving some second gradient models. *Comput. Methods Appl. Mech. Eng.* 193 (27–29), 2771–2796. <http://dx.doi.org/10.1016/j.cma.2003.10.017>.
- Charlier, R., 1987. Approche unifiée de quelques problèmes non linéaires de mécanique des milieux continus par la méthode des éléments finis (grandes déformations des métaux et des sols, contact unilatéral de solides, conduction thermique et écoulements en milieu poreux). Université de Liège, Belgium Ph.D. thesis.
- Coenen, E., Kouznetsova, V., Geers, M., 2011a. Enabling microstructure-based damage and localization analyses and upscaling. *Model. Simul. Mater. Sci. Eng.* 19, 1–15.
- Coenen, E., Kouznetsova, V., Geers, M., 2011b. Novel boundary conditions for strain localization analyses in microstructural volume elements. *Int. J. for Num. Meth. in Eng.* 90, 1–21.
- Collin, F., Chambon, R., Charlier, R., 2006. A finite element method for poro mechanical modelling of geotechnical problems using local second gradient models. *Int. J. Numer. Methods Eng.* 65 (11), 1749–1772.
- Cosserat, E., Cosserat, E., 1909. *Théorie des corps déformables*. Librairie scientifique A. Hermann et fils, Paris, France.
- Coussy, O., 1995. *Mechanics of Porous Continua*. Wiley.
- van den Eijnden, B., 2015. Multiscale modelling of the hydromechanical behaviour of argillaceous rocks. Université Grenoble Alpes Ph.D. thesis.
- El Moustapha, K., 2014. Identification d'une loi de comportement enrichie pour les géomatériaux en présence d'une localisation de la déformation. Université de Grenoble Ph.D. thesis.
- Feyel, F., 2003. A multilevel finite element method (FE2) to describe the response of highly non-linear structures using generalized continua. *Comput. Methods Appl. Mech. Eng.* 192 (28/30), 3233–3244. *Multiscale Computational Mechanics for Materials and Structures*
- Feyel, F., Chaboche, J.-L., 2000. FE² multiscale approach for modelling the elastoviscoplastic behaviour of long fibre sic/ti composite materials. *Comput. Methods Appl. Mech. Eng.* 183 (3–4), 309–330.
- Frey, J., Dascalu, C., Chambon, R., 2012. A two-scale poromechanical model for cohesive rocks. *Acta Geotechnica* 7, 1–18.

- Fritzen, F., Böhlke, T., Schnack, E., 2009. Periodic three-dimensional mesh generation for crystalline aggregates based on Voronoi tessellations. *Comput. Mech.* 43 (5), 701–713.
- Geers, M., Kouznetsova, V., Brekelmans, W., 2010. Multi-scale computational homogenization: Trends and challenges. *J. Comput. Appl. Math.* 234 (7), 2175–2182.
- Germain, P., 1973. La méthode des puissances virtuelles en mécanique des milieux continus. *J. Mécanique* 12, 235–274.
- Geubelle, P., Baylor, J., 1998. Impact-induced delamination of composites: a 2d simulation. *Composites Part B* 29 (5), 589–602.
- Hill, R., 1965. A self-consistent mechanics of composite materials. *J. Mech. Phys. Solids* 13, 213–222.
- Jänicke, R., Diebels, S., Sehlhorst, H.-G., Düster, A., 2009. Two-scale modelling of micro-morphic continua. *Continuum Mech. Thermodyn.* 21 (4), 297–315.
- Jänicke, R., Quintal, B., Steeb, H., 2015. Numerical homogenization of mesoscopic loss in poroelastic media. *Eur. J. Mech. - A/Solids* 49 (0), 382–395.
- Terada, K., Hori, M., Kyoya, T., Kikuchi, N., 2000. Simulation of the multi-scale convergence in computational homogenization approaches. *Int. J. Solids Struct.* 37, 2285–2311.
- Kotrons, P., Al Holo, S., Bésuelle, P., Chambon, R., 2008. Shear softening and localization: Modelling the evolution of the width of the shear zone. *Acta Geotechnica* 3 (2), 85–97.
- Kouznetsova, V., Brekelmans, W.A.M., Baaijens, F.P.T., 2001. An approach to micro-macro modeling of heterogeneous materials. *Comput. Mech.* 27 (1), 37–48.
- Kouznetsova, V., Geers, M., Brekelmans, W., 2004. Multi-scale second-order computational homogenization of multi-phase materials: a nested finite element strategy. *Comp. Methode Appl. Mech. Engg* 193, 5525–5550.
- Mandel, J., 1972. *Plasticité classique et viscoplasticité*. CISM Lecture Notes 97.
- Marinelli, F., van den Eijnden, A., Sieffert, Y., Chambon, R., Collin, F., 2016. Modeling of granular solids with computational homogenization: comparison with biot's theory. *Finite Elements Anal. Design* 119, 45–62.
- Massart, T., Selvadurai, A., 2012. Stress-induced permeability evolution in a quasi-brittle geomaterial. *J. Geophys. Res.* 117, 1–15.
- Massart, T., Selvadurai, A., 2014. Computational modelling of crack-induced permeability evolution in granite dilatant cracks. *Int. J. Rock Mech. Mining Sci.* 70, 593–604.
- Matsushima, T., Chambon, R., Caillerie, D., 2002. Large strain finite element analysis of a local second gradient model: application to localization. *Int. J. for Num. Meth. in Eng.* 54, 499–521.
- Mercatoris, B., Massart, T., Sluys, L., 2014. A multi-scale computational scheme for anisotropic hydro-mechanical couplings in saturated heterogeneous porous media. In: Van Mier, J.G.M., Ruiz, G., Andrade, C., Yu, R.C., Zhang, X.X. (Eds.), *Proceedings of the VIIIth International Conference on Fracture Mechanics of Concrete and Concrete Structures - FraMCoS-8*.
- Mercatoris, B.C.N., Massart, T.J., 2011. A coupled two-scale computational scheme for the failure of periodic quasi-brittle thin planar shells and its application to masonry. *Int. J. Numer. Methods Eng.* 85 (9), 1177–1206.
- Miehe, C., Koch, A., 2002. Computational micro-to-macro transitions of discretized microstructures undergoing small strain. *Arch. Appl. Mech.* 72, 300–317.
- Mindlin, R., 1964. Micro-structure in linear elasticity. *Arch. Rational Mech. Anal.* 16, 51–78.
- Mindlin, R., 1965. Second gradient of strain and surface-tension in linear elasticity. *Int. J. Solids Struct.* 1, 417–438.
- Nguyen, V., Lloberas-Valls, O., Stroeven, M., Sluys, L., 2011. Homogenization-based multiscale crack modelling: from micro-diffusive damage to macro-cracks. *Comput. Methods Appl. Mech. Engng.* 200, 1220–1236.
- Nguyen, V.-D., Noels, L., 2014. Computational homogenization of cellular materials. *Int. J. Solids Struct.* 51 (11–12), 2183–2203.
- Özdemir, I., Brekelmans, W., Geers, M., 2008a. FE² computational homogenization for the thermo-mechanical analysis of heterogeneous solids. *Comput. Methods Appl. Mech. Engng.* 198, 602–613.
- Özdemir, I., Brekelmans, W.A.M., Geers, M.G.D., 2008b. Computational homogenization for heat conduction in heterogeneous solids. *Int. J. Numer. Methods Eng.* 73 (2), 185–204.
- Pijaudier-Chabot, G., Bažant, Z., 1987. Nonlocal damage theory. *J. Eng. Mech.* 113, 1512–1533.
- Schanz, M., 2009. *Poroelastodynamics: linear models, analytical solutions, and numerical methods* 62(3).
- Schröder, J., 2014. *A numerical two-scale homogenization scheme: the FE²-method*. In: *Plasticity and Beyond*, vol. 550. Springer, pp. 1–64.
- van der Sluis, O., Schreurs, P., Brekelmans, W., Meijer, H., 2000. Overall behaviour of heterogeneous elastoviscoplastic materials: effect of microstructural modelling. *Mech. Mater.* 32, 449–462.
- Sonon, B., François, B., Massart, T., 2012. A unified level set based methodology for fast generation of complex microstructural multi-phase (RVEs). *Comput. Methods Appl. Mech. Eng.* 223–224 (0), 103–122.
- Terada, K., Kikuchi, N., 1995. Nonlinear homogenization method for practical applications. *ASME applied mechanics division-publications-AMD*, 212. ASME, pp. 1–16.
- Toro, S., Sánchez, P., Huespe, A., Giusti, S., Blanco, P., Feijóo, R., 2014. A two-scale failure model for heterogeneous materials: numerical implementation based on the finite element method. *Int. J. Numer. Methods Eng.* 97 (5), 313–351.
- Yao, C., Jiang, Q., Shao, J., Zhou, C., 2016. A discrete approach for modeling damage and failure in anisotropic cohesive brittle materials. *Eng. Fracture Mech.*